JASA ARTICLE

Predicting ocean pressure field with a physics-informed neural network

Seunghyun Yoon,[1,2] Yongsung Park,[2,a)] Peter Gerstoft,[2] and Woojae Seong[1,3]

[1]*Department of Naval Architecture and Ocean Engineering, Seoul National University, Seoul 08826, Republic of Korea*

[2]*Scripps Institution of Oceanography, University of California San Diego, La Jolla, California 92093-0238, USA*

[3]*Research Institute of Marine Systems Engineering, Seoul National University, Seoul 08826, Republic of Korea*

ABSTRACT:

Ocean sound pressure field prediction, based on partially measured pressure magnitudes at different range-depths, is presented. Our proposed machine learning strategy employs a trained neural network with range-depth as input and outputs complex acoustic pressure at the location. We utilize a physics-informed neural network (PINN), fitting sampled data while considering the additional information provided by the partial differential equation (PDE) governing the ocean sound pressure field. In vast ocean environments with kilometer-scale ranges, pressure fields exhibit rapidly fluctuating phases, even at frequencies below 100 Hz, posing a challenge for neural networks to converge to accurate solutions. To address this, we utilize the envelope function from the parabolic-equation technique, fundamental in ocean sound propagation modeling. The envelope function shows slower variations across ranges, enabling PINNs to predict sound pressure in an ocean waveguide more effectively. Additional PDE information allows PINNs to capture PDE solutions even with a limited amount of training data, distinguishing them from purely data-driven machine learning approaches that require extensive datasets. Our approach is validated through simulations and using data from the SWellEx-96 experiment. © 2024 Acoustical Society of America.

https://doi.org/10.1121/10.0025235

I. INTRODUCTION

Sound propagation in the ocean has representations governed by physical laws in ocean acoustic environments. A physics-informed neural network (PINN)[1] trains the neural network using sampled data and encodes the underlying physical laws governing the dataset, represented with partial differential equations (PDEs). We present a PINN-based strategy that offers a realistic prediction of ocean acoustic propagation.

In this study, we present OceanPINN, a machine learning framework for predicting ocean acoustic pressure fields. A PINN is fitted to the partially observed experimental data while integrating prior scientific knowledge. OceanPINN utilizes pressure magnitude data from various range-depths for data fitting. Beyond fitting data at known points, OceanPINN enforces the underlying physics of the ocean waveguide, including governing partial differential equation (PDE) and the pressure-release surface boundary condition, which enables extended predictions to unknown points. A sound speed profile (SSP) is required as prior information to compute the governing PDE. Once trained, the OceanPINN can predict the sound pressure field at any given range-depth. The predicted pressure field has a wide range of applications, such as source localization,[2–4] sonar performance assessment,[5,6] and noise prediction for marine mammals.[7,8]

Many papers have adopted machine learning methods for ocean acoustics problems through purely data-driven approaches.[9–19] A few studies have explored integrating physical knowledge into neural networks by applying PINN to estimate modal wavenumbers[20] or by modifying the machine learning framework to satisfy a ray or modal solution.[21,22] Recently, PINN has been applied for underwater pressure prediction.[23] However, the research has focused on an ideal environment with small domain sizes and simple environmental conditions. Our objective is to enable a PINN framework that works in more realistic ocean acoustic environments with kilometer-scale ranges.

Purely data-driven machine learning approaches require extensive training datasets to learn the PDE solutions. In contrast, the PINN-based method encourages the network to learn the structural information expressed by the PDEs, facilitating the network to capture the PDE solutions well, even with a low amount of training data.

PINN has been applied to various fields, including seismology,[24] fluid dynamics,[25] and biophysics.[26] In various acoustic field predictions, PINNs have been employed to solve the Helmholtz[27–29] or wave equation.[30,31] However, these applications involve smaller domain sizes[23,31] or lower frequencies,[27–30] resulting in less complex fields compared to our focus on kilometer-scale real ocean acoustic fields.

Despite the success of PINNs, recent studies[32,33] have shown their limitations in complex PDE problems. Specifically,

a)Email: yongsungpark@ucsd.edu

fully connected neural networks, commonly used in the architecture of PINNs, suffer from a fundamental issue, known as spectral bias.[34] Spectral bias refers to the difficulty in learning high-frequency functions. The spectral bias problem in PINNs[32] was analyzed through neural tangent kernel theory,[35] revealing challenges in learning high-frequency functions.[36] Consequently, applying PINNs to a realistic ocean acoustics environment presents greater challenges due to spectral bias. In our approach, to address this spectral bias, we transform the pressure field into a low-fluctuating representation, called an envelope. OceanPINN is trained to approximate this envelope, with the loss function incorporating the modified Helmholtz equation and pressure-release surface boundary conditions.

Ocean waveguides are typically modeled with two boundary conditions: a pressure-release ocean surface and a bottom with sediment layers. The propagation of acoustic waves within these waveguides is governed by the acoustic wave equation or the Helmholtz equation in the frequency domain. Conventionally, the governing equation is solved using ray theory, normal mode theory, and a parabolic equation model in the ocean environment.[37] The accuracy of acoustic wave field simulations is highly dependent on environmental parameters, including the SSP, bathymetry, and sediment properties. However, the vastness of the ocean can lead to situations with unknown environmental parameters. Direct measurement of sediment properties is challenging and is typically inferred through geoacoustic inversion methods[38–40] from measured acoustic signals. These inversion methods approximate the actual bottom using geoacoustic models, requiring a certain degree of prior knowledge about the bottom in the area of interest.[41,42] The absence of this knowledge can substantially increase the range and number of model parameters needed for analysis. Furthermore, incorrect assumptions about the bottom model can lead to errors in the predicted fields. In contrast, OceanPINN does not require any prior knowledge of the bottom, distinguishing it from conventional model-based geoacoustic inversion methods.

Working with ocean acoustic experimental data presents several challenges. First, array sizes are insufficient to cover the whole ocean waveguide. Additionally, due to the ocean's temporal variability, remeasuring in previously unmeasured areas is complicated, as environmental changes can alter data characteristics. Moreover, accurately measuring the phase in experiments is challenging because of its sensitivity; the phase of ocean acoustic pressure is affected by the Doppler effect[43,44] and varies rapidly across the range. This sensitivity makes range-coherent processing difficult. OceanPINN can address these challenges by predicting unmeasured pressure fields with magnitude data and reconstructing phase information.

In summary, we mitigate the spectral bias in PINNs using the low-fluctuating nature of the envelope that constructs acoustic pressure fields and this enables ocean acoustic pressure field prediction. OceanPINN does not require complex bottom modeling. Additionally, training

OceanPINN with magnitude data enables the reconstruction of phase information, allowing for potential range-coherent processing and improving performance. OceanPINN is evaluated in simulation and experiment conducted in the shallow water evaluation cell experiment 1996 (SWellEx-96).[45,46]

II. PINN-BASED PRESSURE FIELD PREDICTION

In this section, we provide the required background and description of the proposed method. Section II A introduces the governing PDE and discusses the challenges of applying PINN in the ocean waveguide. Section II B explains the data preprocessing method to overcome these challenges. Section II C introduces the general PINN framework, and the proposed PINN-based ocean acoustic pressure field prediction method is described in Sec. II D.

A. Pressure field in the ocean waveguide

The acoustic pressure field satisfies the Helmholtz equation. In an ocean waveguide with a constant-density medium and an azimuth-independent environment, the Helmholtz equation in range-depth coordinates (r, z) is expressed as[37]

$$\frac{1}{r}\frac{\partial}{\partial r}\left(r\frac{\partial p}{\partial r}\right) + \frac{\partial^2 p}{\partial z^2} + \frac{\omega^2}{c^2}p = 0, \tag{1}$$

where ω is an angular frequency, p is a pressure field, and c is a sound speed of medium. The notation (r, z) is abbreviated for variables p and c. The pressure field is obtained by solving the Helmholtz equation with boundary conditions.

Here, we detail the characteristics of the pressure field within an ocean waveguide. For simplicity, a range-independent environment is assumed. Consider a scenario in which a point source is at position (r, z_s) and a single receiver is at position $(0, z)$. The Helmholtz equation is solved with normal mode theory,[37] and the pressure field is a sum of normal modes as

$$p(r, z) = \frac{i}{4\rho(z_s)}\sum_{m=1}^{M}\Psi_m(z_s)\Psi_m(z)H_0^{(2)}(k_m r), \tag{2}$$

where k_m is the mth mode wavenumber, M is the number of propagating modes, and $\Psi_m(z)$ denotes the mth modal depth function. We adopt the second kind Hankel function $H_0^{(2)}(k_m r)$, as we use the Fourier transform pair in the time-frequency (t, f) domain as

$$p(f) = \int_{-\infty}^{\infty} p(t)e^{-i2\pi ft}dt,$$
$$p(t) = \int_{-\infty}^{\infty} p(f)e^{i2\pi ft}df, \tag{3}$$

where the sign of the phase in the exponent term is opposite to Ref. 37. Mode wavenumbers are determined by environmental parameters (e.g., SSP and geoacoustic parameters).

We can compute the mode wavenumber in the perfectly known environment and generate the pressure field.

Hankel function $H_0^{(2)}(k_m r)$ determines the pressure variation in range direction as Eq. (2). In the far field ($kr \gg 1$), the Hankel function form is asymptotic,

$$H_0^{(2)}(kr) \approx \sqrt{\frac{2}{\pi kr}} e^{-i(kr-\pi/4)}. \tag{4}$$

The phase of the Hankel function changes rapidly with slight range variations, causing the pressure field to exhibit rapid variations with respect to range. In contrast, the magnitude of the Hankel function, i.e., $\sqrt{2/\pi kr}$ changes slowly with respect to range. In Fig. 1, we present an example of a simulated pressure field using the Kraken normal mode model[47] in an isovelocity environment (see Sec. IV A for detail). As seen in Figs. 1(c) and 1(e), the real and imaginary component of the pressure field exhibits rapid variation with respect to range, while the magnitude changes gradually, as shown in Fig. 1(a). This characteristic of complex pressures presents two challenges: (1) The highly fluctuating patterns make training neural networks challenging. (2) Even a small error in range, denoted as Δr, results in a significant difference between the measured pressures $p(r, z)$ and $p(r + \Delta r, z)$. We can mitigate the second challenge by using the magnitude of measured pressure $|p|$ with lower sensitivity. The approach to address the first challenge is detailed in the subsequent section.

B. Smoothing the pressure field

To address the first challenge, we adopt an envelope $\psi(r, z)$ used in the derivation of the parabolic equation,[37]
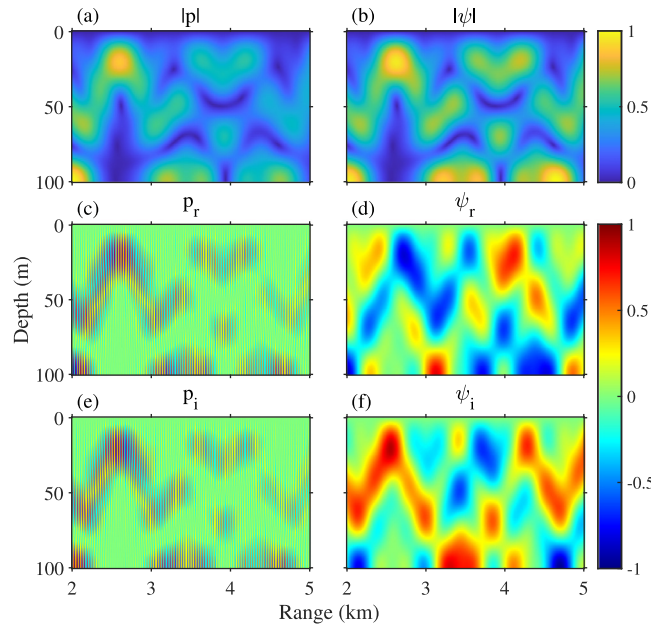

FIG. 1. (Color online) Normalized (a) and (b) magnitude, (c) and (d) real, and (e) and (f) imaginary of pressure field (left) and envelope field (right). The data are simulated in an isovelocity environment with a 100 Hz source at 25 m depth.

and smooth the pressure field. The envelope $\psi(r, z)$ is defined by Eq. (6.3) of Ref. 37,

$$\psi(r, z) = p(r, z)/H_0^{(2)}(k_0 r), \tag{5}$$

where $k_0 = \omega/c_0$ is the reference wavenumber, c_0 is the reference sound speed, which is 1500 m/s. We name Eq. (5) as the envelope transform. In an ocean waveguide, the acoustic pressure field is dominated by modes with close mode wavenumbers. Mode wavenumber can be expressed as $k_m = \omega/c_m$, where c_m represents the phase velocity of mth mode. Since c_0 is close to c_m, k_0 is close to k_m, and an envelope transform can smooth the acoustic pressure field by decreasing a wavenumber to $k_m - k_0$. Figures 1(d) and 1(f) show a real and imaginary component of envelope ψ, exhibiting much smoother variation compared to the pressure field in Figs. 1(c) and 1(e). If c_0 is adjusted to reduce further $|k_m - k_0|$, a smoother envelope field is achieved. However, since $c_0 = 1500$ m/s significantly reduces the wavenumber, further adjustment yields marginal effects. Since the range of c_m is unknown, we set c_0 as 1500 m/s.

To overcome the second challenge, we use the magnitude of the envelope, which is easily converted from the magnitude of the pressure field. In far-field condition ($kr \gg 1$), the magnitude of the envelope is expressed as

$$|\psi(r, z)| = \sqrt{\frac{\pi k_0 r}{2}} |p(r, z)|. \tag{6}$$

Figure 1(b) shows the envelope magnitude. Unlike the pressure magnitude in Fig. 1(a), the envelope magnitude does not decrease with range, as it is compensated by a factor of $\sqrt{r}$.

The governing equation for envelope ψ is derived: Rewriting the Helmholtz equation in Eq. (1) as

$$\frac{\partial^2 p}{\partial r^2} + \frac{1}{r}\frac{\partial p}{\partial r} + \frac{\partial^2 p}{\partial z^2} + k_0^2 n^2 p = 0, \tag{7}$$

where $n(r, z) = c_0/c(r, z)$ is the index of refraction. Substituting the pressure p into Eq. (7) by envelope ψ, and using that the Hankel function, satisfies the Bessel differential equation,[37]

$$\frac{\partial^2 H_0^{(2)}(k_0 r)}{\partial r^2} + \frac{1}{r}\frac{\partial H_0^{(2)}(k_0 r)}{\partial r} + k_0^2 H_0^{(2)}(k_0 r) = 0, \tag{8}$$

gives

$$\frac{\partial^2 \psi}{\partial r^2} + \left(\frac{2}{H_0^{(2)}(k_0 r)}\frac{\partial H_0^{(2)}(k_0 r)}{\partial r} + \frac{1}{r}\right)\frac{\partial \psi}{\partial r} + \frac{\partial^2 \psi}{\partial z^2} + k_0^2(n^2 - 1)\psi = 0. \tag{9}$$

Using Eq. (4), the governing equation for envelope function ψ is derived as[37]

$$\mathcal{N}_\psi[\psi] \stackrel{\text{def}}{=} \frac{\partial^2 \psi}{\partial r^2} - 2ik_0 \frac{\partial \psi}{\partial r} + \frac{\partial^2 \psi}{\partial z^2} + k_0^2(n^2 - 1)\psi = 0, \tag{10}$$

where $\mathcal{N}_\psi$ represents differential operator.

C. Physics-informed neural networks

PINN is a deep-learning framework for solving forward and inverse problems involving nonlinear PDEs.[1] PINN deals with general physics systems, characterized by a governing equation, Eq. (11), and a boundary condition, Eq. (12), that are satisfied within a domain Ω along its boundary $\partial\Omega$,

$$\mathcal{N}[u(x)] = f(x) \quad x \in \Omega, \tag{11}$$

$$\mathcal{B}[u(x)] = g(x) \quad x \in \partial\Omega, \tag{12}$$

where x represents input coordinates, such as spatial and temporal dimensions, while u represents physical quantities, as pressure or velocity. $\mathcal{N}[\cdot]$ and $\mathcal{B}[\cdot]$ denote differential operator. Neural networks are universal function approximators,[48] capable of representing any continuous function with the proper configuration and a sufficient number of neurons. For PINN, neural networks are used to approximate the solutions of PDEs, $u(x)$ (see Fig. 2).

A limited set of input–output pairs $\{x_m^i, u(x_m^i)\}_{i=1}^{N_m}$ is known, obtained from initial conditions or measurements. There are three sources of information to solve the problem: (1) a limited number of known input–output pairs, (2) the governing equation, and (3) the boundary condition. It is important to note that even with limited data, leveraging the system's underlying physics allows us to compensate for sparse datasets. Contrasting with purely data-driven machine learning methods that depend solely on a limited dataset of input–output pairs, PINNs integrate physical principles into their loss function. This integration enables the PINN to effectively solve problems, even with a small amount of dataset.

PINNs are trained with a composite loss function,

$$\mathcal{L}(\theta) = \lambda_M \mathcal{L}_\mathcal{M}(\theta) + \lambda_B \mathcal{L}_\mathcal{B}(\theta) + \lambda_N \mathcal{L}_\mathcal{N}(\theta), \tag{13}$$

where λ_M, λ_B, and λ_N are weighting coefficients and θ is trainable parameters of neural network. Neural network parameters are updated using gradient-descent methods based on the backpropagation of the loss function. Each loss term is expressed as

$$\mathcal{L}_\mathcal{M}(\theta) = \frac{1}{N_m} \sum_{i=1}^{N_m} \left| \hat{u}(x_m^i; \theta) - u(x_m^i) \right|^2, \tag{14}$$

$$\mathcal{L}_\mathcal{B}(\theta) = \frac{1}{N_b} \sum_{i=1}^{N_b} \left| \mathcal{B}[\hat{u}(x_b^i; \theta)] - g(x_b^i) \right|^2, \tag{15}$$

$$\mathcal{L}_\mathcal{N}(\theta) = \frac{1}{N_n} \sum_{i=1}^{N_n} \left| \mathcal{N}[\hat{u}(x_n^i; \theta)] - f(x_n^i) \right|^2. \tag{16}$$
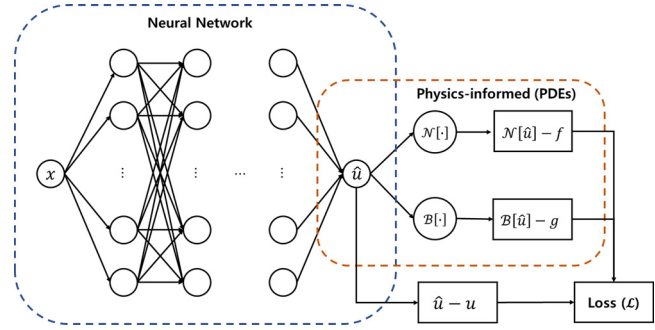
FIG. 2. (Color online) The general PINN framework.

$\mathcal{L}_\mathcal{M}$, $\mathcal{L}_\mathcal{B}$, and $\mathcal{L}_\mathcal{N}$ have a distinct role: fitting the neural network to the known data, enforcing the boundary condition, and the governing equation. Traditional neural networks rely solely on a data-based loss function, $\mathcal{L}_\mathcal{M}$. In contrast, PINNs incorporate physics-based losses, $\mathcal{L}_\mathcal{B}$ and $\mathcal{L}_\mathcal{N}$. These losses are evaluated at different sets of data points, including known points $\{x_m^i\}_{i=1}^{N_m}$, boundary points $\{x_b^i\}_{i=1}^{N_b}$, and collocation points $\{x_n^i\}_{i=1}^{N_n}$. Boundary and collocation points are specific sampling locations to enforce the boundary condition and the governing PDE. These points are strategically sampled from the boundary $\partial\Omega$ and the domain Ω of the physics problem, respectively. The number of these sampling points, N_n for collocation and N_b for boundary points, can be freely selected. The differential operator $\mathcal{B}[\cdot]$ and $\mathcal{N}[\cdot]$ can be easily calculated since neural networks can efficiently compute gradients of the outputs with respect to the inputs, $\partial\hat{u}/\partial x$, via automatic differentiation.[49] This enables computing loss terms $\mathcal{L}_\mathcal{B}$ and $\mathcal{L}_\mathcal{N}$.

D. OceanPINN

We propose OceanPINN, an approach that harnesses PINN[1] to reconstruct the unmeasured acoustic field in ocean waveguides, using partially measured data. Due to the sensitivity of the phase, we exclusively use the magnitude from the measured data. As depicted in Fig. 3(a), acoustic magnitudes are transformed into envelope magnitudes using Eq. (6) before training.

In the OceanPINN, the fully connected neural network receives a range-depth (r, z) as input and outputs the real and imaginary envelope $\hat{\psi}_r(r, z)$ and $\hat{\psi}_i(r, z)$ at the input location (r, z), as Fig. 3(c). The complex envelope is formed from these outputs as $\hat{\psi} = \hat{\psi}_r + i\hat{\psi}_i$. After training, the neural network generates the envelope $\hat{\psi}(r, z)$ for specific points (r, z). The pressure field $\hat{p}(r, z)$ is then estimated by multiplying the estimated envelope $\hat{\psi}(r, z)$ with the Hankel function $H_0^{(2)}(k_0 r)$.

A fully connected neural network with L hidden layers, an input layer (layer 0), and an output layer (layer $L + 1$) is used for the OceanPINN [see Fig. 3(c)]. We apply the sine activation functions because it is effective in representing the complex signals and their derivative.[50] In addition,

adopting sine activation is effective for solving the Helmholtz Equation.[27,50] The network can be expressed as

$$x_{l+1} = \begin{cases} \sin(W_l x_l + b_l), & l = 0, \ldots, L-1, \\ W_l x_l, & l = L, \end{cases} \tag{17}$$

where x_l denotes the lth layer and W_l and b_l denote the weight and bias connecting the layer l and $l+1$.

We use three sources of information: (1) measured data, (2) the governing equation [Eq. (10)], and (3) the pressure release surface boundary condition with $\psi(r, 0) = 0$. Each information is incorporated into the loss function as

$$\mathcal{L}_\mathcal{M} = \frac{1}{N_m} \sum_{i=1}^{N_m} |\hat{\psi}_r^2(r_m^i, z_m^i) + \hat{\psi}_i^2(r_m^i, z_m^i) - |\psi(r_m^i, z_m^i)|^2|, \tag{18}$$

$$\mathcal{L}_\mathcal{B} = \frac{1}{N_b} \sum_{i=1}^{N_b} |\hat{\psi}(r_b^i, 0)|^2, \tag{19}$$

$$\mathcal{L}_\mathcal{N} = \frac{1}{N_n} \sum_{i=1}^{N_n} |\mathcal{N}_\psi[\hat{\psi}(r_n^i, z_n^i)]|^2. \tag{20}$$

Here, neural network parameters θ are omitted for simplicity. Note that in Eq. (18), since only the magnitude of the measured data is available, the neural network outputs are compared with the magnitude square. Losses are combined as in Eq. (13) and used to train OceanPINN.

Training points are depicted in Fig. 3(c). Boundary points are evenly sampled from the water surface, and collocation points are sampled from the water medium differently in each iteration to prevent the PINN from being trapped in local minima.[51] Further details on the sampling method for collocation points are shown in Appendix A.

We utilize the following hyperparameters: loss weight coefficients are set as $\lambda_M = 1$, $\lambda_N = 10^5$, $\lambda_B = 1$. Further

details for loss weight coefficients are provided in Appendix B. The number of training points, N_n and N_b, are set to 3000 and 100, respectively. The network architecture comprises $L = 5$ hidden layers, each with 160 neurons. The loss function is optimized using the Adam optimizer with a learning rate of 10^{-4}. We multiplied the loss function by 10^4 arbitrarily, which improved the convergence speed and model performance of analyzed cases. This adjustment aims to prevent overly small gradients, reducing the likelihood of the model falling into local minima.

III. ISOVELOCITY PROBLEM

This section evaluates and compares the performance of OceanPINN with other representative machine-learning frameworks. We consider a simple problem characterized by an isovelocity profile, constant density, and boundary conditions including a pressure-release surface and a rigid bottom, as outlined in Chapter 5.4 of Ref. 37 (see Fig. 4). The acoustic pressure field is generated using Eq. (5.49) from Ref. 37. The first four of the 13 propagating modes are considered for simulation following the example presented in Refs. 37 and 52. The pressure field is generated across a range of 2–5 km. The sound pressure level (SPL) of the simulated pressure field is presented in Fig. 5(a), which is normalized by its maximum value.

To assess the predictive performance in unsampled range-depths, we sample pressure magnitudes while excluding certain depths and ranges. For depth, pressure magnitudes are sampled at 5 m intervals, specifically between 5 and 30 m and 80–95 m. For ranges, pressure magnitudes are sampled at 25 m intervals over 600 m, and the next 400 m is unsampled. This pattern is repeated. Dashed boxes in Figs. 5(b)–5(d) illustrate the sampled regions.

The predictive performance is quantitatively assessed by the mean absolute error (MAE) of SPL, defined as
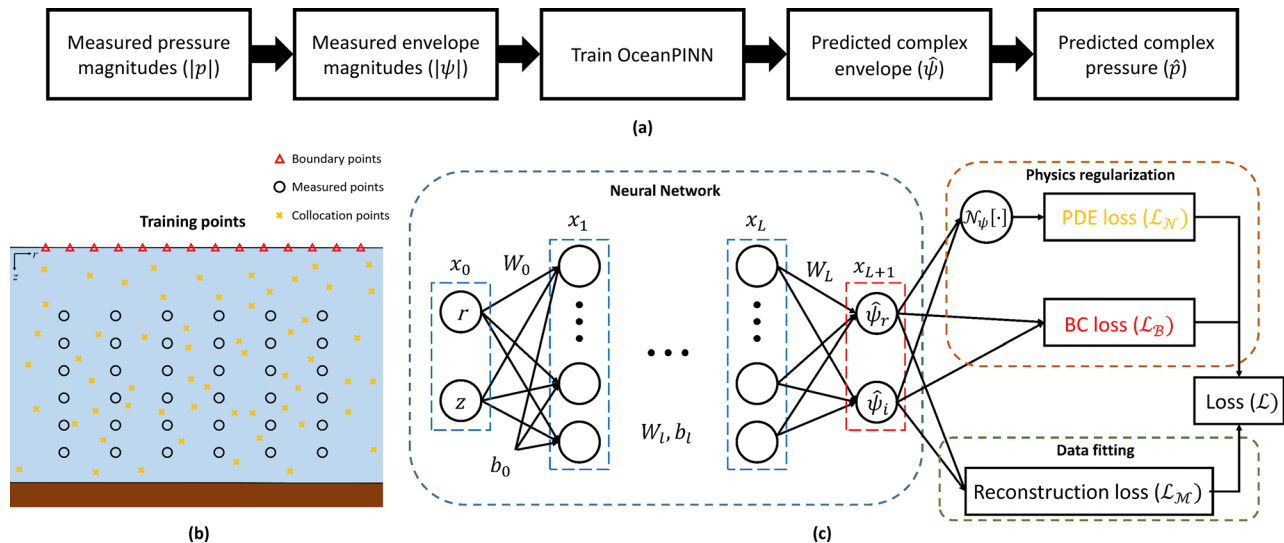

FIG. 3. (Color online) (a) Flowchart, (b) training points, (c) schematic of the OceanPINN.
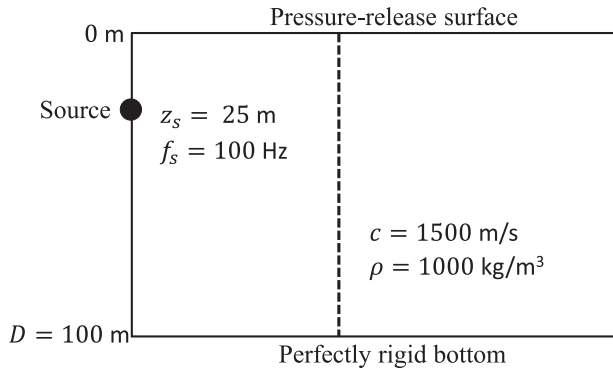
J. Acoust. Soc. Am. **155** (3), March 2024

Yoon et al.   2041

FIG. 4. Schematic of the isovelocity problem.

$$\text{MAE} = \frac{1}{n}\sum_{i=1}^{n} |L_p^i - \hat{L}_p^i|, \qquad (21)$$

where $\hat{L}_p$ and L_p are the predicted and true SPL, n is the total number of evaluated points, and i indexes the individual points. For the isovleocity problem, evaluation points are uniformly distributed on the (r, z) grid at 10 m and 1 m intervals, respectively. Surface points are excluded due to the SPL being negative infinity, i.e., $p(r, 0) = 0$.

A. Results

Three machine learning methods are evaluated, including the proposed OceanPINN. Two methods are compared with OceanPINN, all employing the same neural network architecture but differing in their outputs and loss functions. Specifically, whereas OceanPINN outputs the envelope $\hat{\psi}$, two other methods output the pressure $\hat{p}$. The first method for comparison is a purely data-driven approach, trained solely using reconstruction loss where ψ of Eq. (18) is replaced by p. The second method for comparison is a PINN that outputs the pressure. This method is trained with composite loss similar to OceanPINN, which replaces the ψ to p in Eq. (18) and Eq. (19), and Eq. (20) is revised to enforce the original Helmholtz equation in Eq. (7). To keep the loss functions on equal footing, we empirically choose $\lambda_M = \lambda_N = \lambda_B = 1$, in agreement with Ref. 23.

These methods are trained over 500 000 epochs using pressure magnitude samples, and after training, they predict the complex pressure field in the entire domain. The magnitude of the predicted pressure field and the phase difference from the true field are presented in Figs. 5(b)–5(d). The SPL figures are normalized to the maximum value of the true pressure field. The homogeneous Helmholtz equation allows multiple solutions with constant phase shifts θ. For instance,
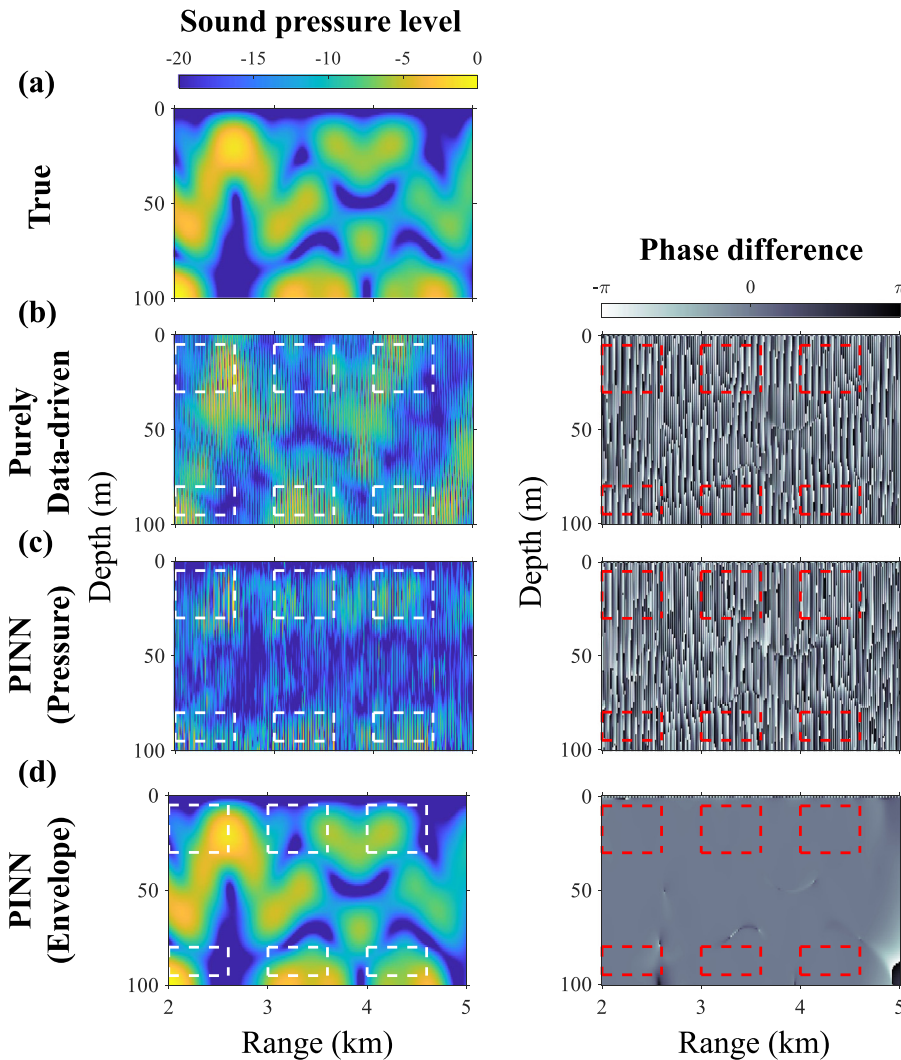

FIG. 5. (Color online) (Left) The normalized sound pressure level (dB), (Right) phase difference between true and predicted pressure field. Each row illustrates (a) true, (b) purely data-driven method, (c) PINN with pressure output, (d) PINN with envelope output (OceanPINN). Dashed boxes represent the sampled region.

if $p(r, z)$ is a solution, then $p(r,z)e^{i\theta}$ is a valid solution. Since phase information is not provided, the predicted field can exhibit a constant phase difference from the true field. Note that these predictions with a constant phase difference, still qualify as PDE solutions and are spatially coherent.

Figures 5(b) and 5(c) present the prediction results of the compared methods, showing significant discrepancies from the true values in both magnitude and phase. The predicted SPLs in Figs. 5(b) and 5(c) are inaccurate even in the sampled region. This inaccuracy is attributed to the relatively sparse sampling intervals, which are insufficient for neural networks to capture the highly fluctuating nature of complex ocean acoustic pressure fields. In contrast, OceanPINN predictions in Fig. 5(d) are accurate in both magnitude and phase. The proposed method achieves significantly lower MAE than other methods, as shown in Table I. The phase differences are consistent across the entire region, except in the small areas where the magnitude is close to zero, where we can neglect the phase. These results demonstrate the effectiveness of the proposed PINN framework using the envelope field. However, OceanPINN also exhibits inaccuracies around 5 km, near the bottom, highlighting the inherent challenges PINNs face with extrapolation.[53]

IV. SWELLEX-96

We evaluate the OceanPINN in a more realistic environment. The analysis utilizes both simulation and experimental data from the SWellEx-96 Event S5[54–57] environment, which was conducted at 23:15–00:30 UTC from May 10–11, 1996. A brief overview of the SWellEx-96 experiment and the specific source-receiver configuration used for the training data is provided.

During the experiment, the source ship simultaneously towed two sources: the shallow source and the deep source, each transmitting different multi-tonal sets. Here, we focus on the 109 Hz shallow source towed at a 9 m depth. The data were recorded by a 64-element VLA spanning depths of 94.125–212.25 m. A subset of the VLA comprising 13 evenly spaced elements (from elements 1–61) was selected for constructing the training dataset. The dataset incorporates data from transmissions originating between 1.5 and 3.5 km from the VLA, excluding ranges of 2.1–2.3 km and 2.7–2.9 km. Source-receiver configuration for training data is illustrated in Fig. 6(a).

We assumed a range-independent environment, consistent with previous studies.[43,44,52,58] With N_r range samples and 13 hydrophones, we can obtain $N_r \times 13$ different magnitude pressure field measurements, denoted as $|p(r_i, z_j)|$ for $1 \leq i \leq N_r, 1 \leq j \leq 13$, where r_i represents the distance

TABLE I. MAE of the predicted pressure field in Figs. 5(b)–5(d).

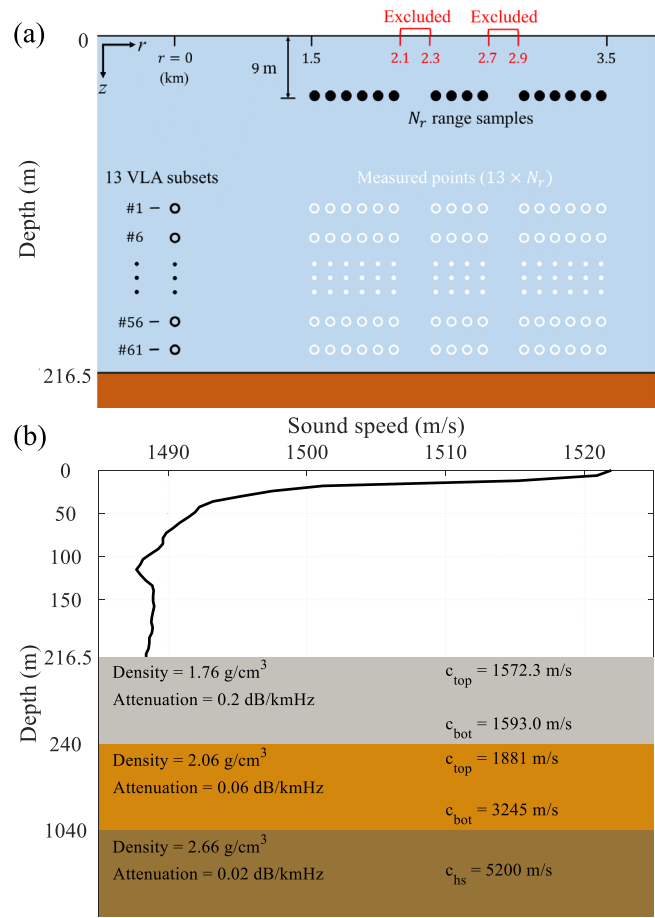| Method	MAE (dB)
Purely data-driven	5.65
PINN (Pressure)	7.58
OceanPINN	0.50

FIG. 6. (Color online) (a) Source-receiver configuration for the training dataset, (b) environmental parameters of the SWellEx-96 experiment.

between the ith transmission source and jth hydrophone at depth z_j. These measurement points are illustrated as white points in Fig. 6(a). The number of range samples, N_r differs between simulation and experiment. The measured pressure magnitude $|p|$ is converted to the envelope magnitude $|\psi|$ according to Eq. (6) and used to train OceanPINN.

A. SWellEx-96 simulation data generation

In the simulation, the data are sampled in 20 m range intervals and yields a total of $N_r \times N_z = 83 \times 13$ samples for training. We used the Kraken normal mode model[47] to simulate the acoustic pressure field. Bottom attenuation influences the effective mode cutoff, and using an incorrect number of propagating modes can lead to mismatches between replicas and experimental data.[55,59] Accordingly, we conducted SWellEx-96 109 Hz simulations using 14 modes, as in the experimental data. The environmental parameters used for simulation are illustrated in Fig. 6(b).

OceanPINN is assessed across various signal-to-noise ratios (SNRs) of 12 and 6 dB, including noiseless conditions. In noisy scenarios, Gaussian noise is added to the generated pressure data. SNR is defined as

$$SNR = 20 \log_{10} \frac{||P_s||_F}{||P_n||_F}, \qquad (22)$$

where $||\cdot||_F$ is Frobenius norm, and $P_s \in \mathbb{C}^{N_r \times N_z}$ and $P_n \in \mathbb{C}^{N_r \times N_z}$ represent the noiseless measurement and additive noise at N_r range samples and N_z depth samples.

B. SWellEx-96 simulation results

OceanPINN is trained over 1 200 000 epochs. After training, the pressure field is generated on a uniform (r, z) grid. The grid spans from 1 to 4 km for r at 10 m intervals and from 0 to 216.5 m for z with 300 uniformly spaced points.

Figures 7(b)–7(d) present predicted pressure magnitude fields, beamformings, and phase differences by OceanPINN, trained with data from various SNRs. All pressure magnitude figures are normalized to the maximum value of the true pressure field, and the beamforming figures are scaled to their maximum values. For easier comparison, each phase difference figure has been shifted by a constant phase to make the average phase difference zero.

The predicted SPLs from OceanPINN are consistent with the true field across all SNRs. However, as previously discussed in Sec. IV A, discrepancies are observed in the extrapolated range of 3.5–4 km. Table II provides a detailed quantitative analysis. MAEs increase in every SNRs as the predicted range extends from 1.5–3.5 km to 1–4 km.

We validated the physical consistency of the predicted pressure field by the direction of arrival (DOA) in the beamforming figures.[54,56] We applied conventional beamforming to the predicted pressure fields. OceanPINN accurately predicts DOA within the interpolated range of 1.5–3.5 km, affirming the physical consistency of its pressure field predictions. However, beamforming results of OceanPINN show discrepancies at 3.5–4 km, showing limitations in extrapolating over longer ranges.

The phase differences depicted in Figs. 7(b) –7(d) are nearly zero across the entire region within the interpolated range of 1.5–3.5 km, indicating precise phase estimation. Discontinuities in these figures correspond with regions where the pressure magnitude is negligible or zero, which leads to phase values becoming indeterminate. In noisy conditions, such discontinuities become more prominent, since noise can mask the low-magnitude areas. In the extended range, the phase error increases, also showing challenges in range extrapolation.
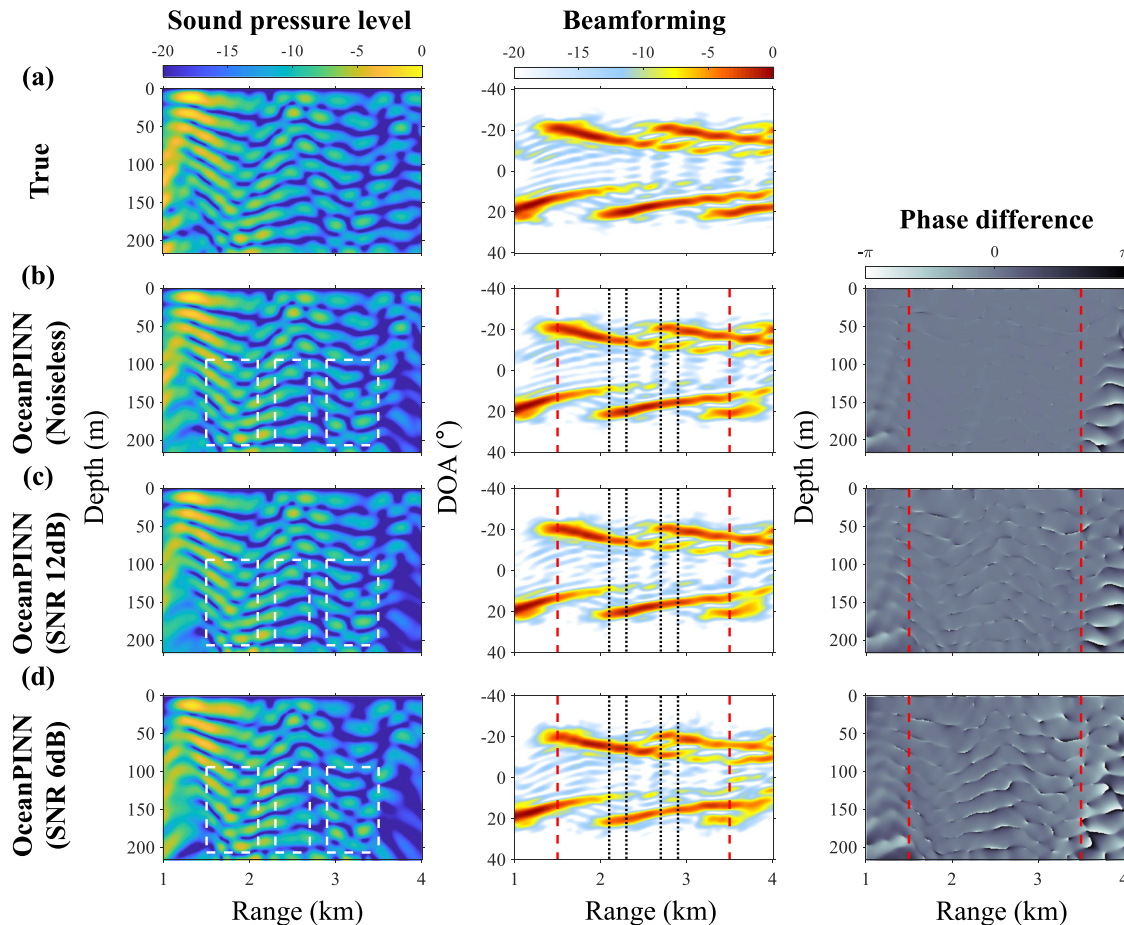

FIG. 7. (Color online) (Left) The normalized sound pressure level (dB), (Middle) beamforming (dB), and (Right) phase difference between true and predicted pressure field. Each row illustrates (a) true and OceanPINN prediction using (b) noiseless, (c) SNR 12 dB, (d) SNR 6 dB simulation data. Dashed and dotted lines represent the boundaries of sampled data.

2044   J. Acoust. Soc. Am. 155 (3), March 2024

Yoon et al.

TABLE II. MAE of the predicted pressure field in Figs. 7(b)–7(d): Evaluated in the interpolated range of 1.5–3.5 km and the extended range of 1–4 km.

	MAE (dB)	
Meausurement SNR	1.5–3.5 km	1–4 km
Noiseless	0.18	0.68
12 dB	0.87	1.44
6 dB	1.83	2.38

C. SWellEx-96 experimental data

SWellEx-96 data are recorded by the VLA at a sampling rate of 1500 Hz. Due to data corruption, the data from the 22nd hydrophone are excluded from the analysis. Global positioning system (GPS) data from the tow ship and the VLA are used to estimate ranges and synchronize the corresponding time. We analyze data recorded at 23:50–00:06 UTC, which corresponds to distances of 3.7–1.3 km from the VLA. Note that the ship was moving closer to the VLA during this period.

The signal is divided into 817 snapshots, each 2.73 s (2^{12} samples) long, with a 50% overlap. These snapshots are then analyzed using a fast Fourier transform (FFT). Due to the towed source in the SWellEx-96 experiment, the measurements were affected by the Doppler shift.[43,52] To account for Doppler offset, we select the FFT bin with the maximum power within the range of 109 ± 0.5 Hz.

From the entire processed data, a specific subset is selected for the training dataset, which follows the source-receiver configuration depicted in Fig. 6(a), consistent with the simulation analysis. The only difference lies in the number of range samples N_r. For range samples, the training
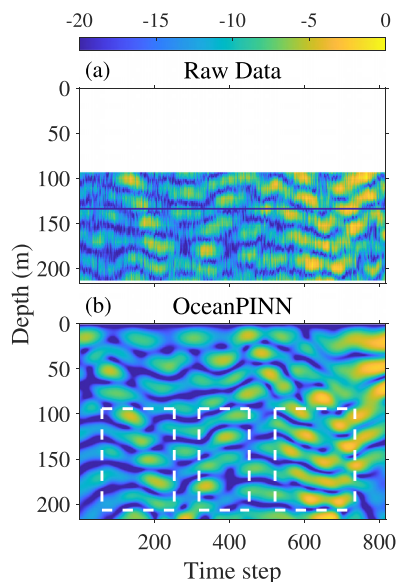

FIG. 8. (Color online) Normalized sound pressure level (dB) of (a) raw data, (b) OceanPINN predicted data with the boundaries of measurements indicated (white boxes).
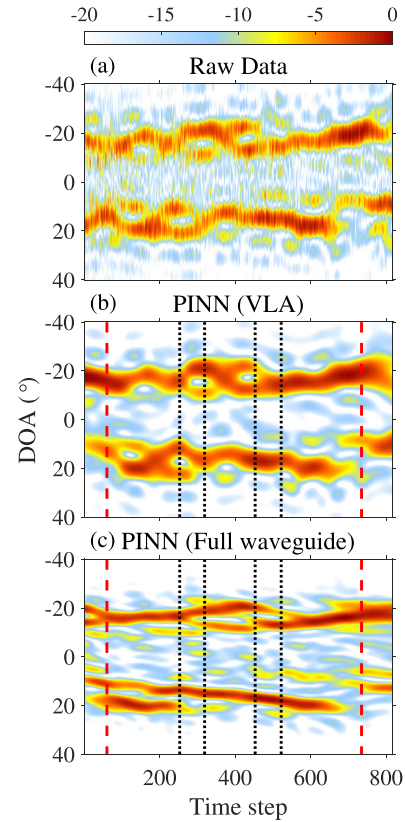

FIG. 9. (Color online) Conventional beamforming (dB) from (a) raw data, (b) OceanPINN predictions within VLA depth, (c) across the full water column. The measurement boundaries are at 1.5 and 3.5 km (black dashed), while the excluded sections are at 2.1–2.3 and 2.7–2.9 km (red dotted).

dataset encompasses snapshots from 3.5 km (61st snapshot) to 1.5 km (736th snapshot) relative to the VLA but excludes data from the ranges of 2.1–2.3 km and 2.7–2.9 km, yielding a total of $N_r = 537$ samples. For receiver configuration, the training dataset consistently utilizes a uniformly spaced subset of 13 elements (elements 1–61).

D. SWellEx-96 experimental results

OceanPINN is trained over 1 200 000 epochs. Once OceanPINN is trained, the pressure field is generated on a uniform (r, z) grid. Here, r corresponds to the range of each snapshot, and z consists of 300 uniformly distributed points spanning the full water column 0–216.5 m.

Figure 8 illustrates the normalized SPLs of the raw data and the OceanPINN prediction, normalized with respect to the maximum of the raw data. The data from the 22nd element [black line in Fig. 8(a)] is excluded from the analysis due to corruption. The SPL increases over time since the source approaches. Comparisons are confined to the VLA region due to no measurements above it. The OceanPINN predictions show a good agreement with the experimental data within the interpolated range (1.5–3.5 km), including the excluded parts not used for training. Nevertheless, discrepancies are noted in some parts of the extrapolated range. Additionally, the OceanPINN-predicted pressure field exhibits reduced noise features compared to the raw data.

J. Acoust. Soc. Am. **155** (3), March 2024

Yoon *et al.*   2045

We validate the physical consistency of OceanPINN predictions by comparing their DOA using conventional beamforming. This comparison allows us to indirectly validate the predictions in unmeasured regions above the VLA. The beamforming is normalized by the maximum value. Figure 9 shows the beamforming from raw data, OceanPINN prediction within VLA depth, and OceanPINN prediction for the whole water column. The DOA from OceanPINN prediction shows good agreement with raw data. Similar to the magnitude, the interpolated range (1.5–3.5 km) showed consistency, while the extrapolated range showed slight differences. Since the array aperture length is identical in Figs. 9(a) and 9(b), beamforming results show the same resolution. While Fig. 9(c) uses an extended array, it shows improved angular resolution, and can distinguish multipath. The results indicate that the OceanPINN prediction is consistent physically. Moreover, akin to Fig. 8, the noisy feature is decreased in the beamformings from OceanPINN predictions.

V. CONCLUSION

We introduced an approach named OceanPINN, which uses the PINN for predicting acoustic pressure fields in ocean waveguides from partially measured data. OceanPINN can be considered a method that performs interpolation and extrapolation from a few sampled points based on physics knowledge. Specifically, the neural network is trained with a physics-based loss that enforces the governing equation and the surface-boundary condition.

The rapid phase variations of the complex pressure field in the ocean acoustic environment pose two challenges for applying the PINN framework. The first is spectral bias, which we mitigated by transforming the high-wavenumber pressure field into a low-wavenumber envelope. The second is the inaccuracy of phase measurements; we addressed this by training solely on the magnitude of the measured pressure data.

The simulations indicated that OceanPINN can accurately predict unmeasured pressure fields. Moreover, results show that OceanPINN can infer phase information solely from magnitude data. In real data applications, OceanPINN predictions match well with VLA measurements and show physically consistent predictions, even above the VLA, which is unmeasured in the experiment. However, the performance of OceanPINN degrades in the extrapolated range, both in simulations and experimental data, which is possibly an inherent weakness of PINNs.

ACKNOWLEDGMENTS

AUTHOR DECLARATIONS
Conflict of Interest

The authors have no conflicts to disclose.

DATA AVAILABILITY

The data that support the findings of this study are available from the corresponding author upon reasonable request.

APPENDIX A: COLLOCATION POINT SAMPLING

Within the PINN framework, the correct solution is known only at a few points. The values at the remaining unknown points are deduced by minimizing the PDE residual defined as

$$\mathcal{R}(\theta) = \mathcal{N}[\hat{u}(x;\theta)] - f(x) \tag{A1}$$

in the general PINN framework in Sec. II C. However, it is important to note that a small PDE residual does not necessarily imply a correct solution. For instance, in our problem, a trivial solution of $\psi(r,z) = 0$ also effectively minimizes the PDE residual. According to Ref. 51, for training PINNs to converge correctly, the correct solution needs to propagate from known points to unknown points throughout iterations. Failure in this propagation can lead subsequent points to convergence to the trivial solution. The PDE residual calculated at a specific collocation point is influenced only by nearby values, and if these nearby values are incorrect, that local region can exhibit a low PDE residual even if it is not a correct solution. Such a failure in propagation is also observed in OceanPINN. As seen in Fig. 7(d), in a far extrapolated range near 4 km, the predicted pressure field shows a trivial solution of $p(r,z) = 0$ in several areas.

As training progresses, PINN can be converged to solutions that have two distinct regions: one region converges to the correct solutions, while the other converges to trivial solutions. Although both regions show low PDE residuals, the narrow boundary between them is likely to exhibit high PDE residuals. However, since PDE loss is averaged over all collocation points, the loss remains small, if collocation points are uniformly distributed and most areas show low PDE residuals. This can lead to challenges in updating and getting stuck in local minima. We adopt Retain-Resample-Release (R3) sampling,[51] which accumulates collocation points in high PDE residual regions to address this problem. Specifically, R3 sampling determines collocation points by retaining half of the points with high PDE residuals from the previous iteration and resampling the other half from a uniform random distribution.

As OceanPINN has a real and imaginary output, during a training process, the real (R_r) and imaginary (R_i) PDE residuals are computed separately for collocation point $\{r_n^i, z_n^i\}_{i=1}^{N_n}$, and summed for calculating PDE loss $\mathcal{L}_{\mathcal{N}}$ as

$$\mathcal{L}_{\mathcal{N}}(\theta) = \frac{1}{N_n} \sum_{k=1}^{N_n} |R_r^k(\theta) + iR_i^k(\theta)|^2, \tag{A2}$$

$$R_r^k(\theta) = \frac{\partial^2 \hat{\psi}_r^k}{\partial r^2} + 2k_0 \frac{\partial \hat{\psi}_i^k}{\partial r} + \frac{\partial^2 \hat{\psi}_r^k}{\partial z^2} + k_0^2(n^2 - 1)\hat{\psi}_r^k, \qquad \text{(A3)}$$

$$R_i^k(\theta) = \frac{\partial^2 \hat{\psi}_i^k}{\partial r^2} - 2k_0 \frac{\partial \hat{\psi}_r^k}{\partial r} + \frac{\partial^2 \hat{\psi}_i^k}{\partial z^2} + k_0^2(n^2 - 1)\hat{\psi}_i^k, \qquad \text{(A4)}$$

where superscript k denotes corresponding to the kth collocation point.

We aim to accumulate collocation points with either high real or imaginary PDE residuals to achieve a balance between the real and imaginary residuals of the PDE. The pseudo-code of the sampling method for collocation points is described in Algorithm I.

APPENDIX B: LOSS WEIGHT COEFFICIENTS

PINNs utilize a composite loss function comprising physics-based loss and data-fitting terms. The general form of the PINN composite loss function can be represented as

$$\mathcal{L}(\theta) = \sum_{i=1}^{M} \lambda_i \mathcal{L}_i(\theta). \qquad \text{(B1)}$$

With this loss function, neural network parameters θ are typically updated with the gradient descent as[60]

$$\theta_{n+1} = \theta_n - \eta \sum_{i=1}^{M} \lambda_i \nabla_\theta \mathcal{L}_i(\theta_n), \qquad \text{(B2)}$$

where η denotes the learning rate. Disparities in the gradients of these loss terms can lead to discrepancies in the convergence rates of each component. Disparities in the gradients of each loss term $\nabla_\theta \mathcal{L}_i(\theta_n)$ can lead to discrepancies in the convergence rates of each component.[36,60] Loss weight coefficients address this issue, as they rescale the learning rate of each loss term $\mathcal{L}_i$ to $\eta \lambda_i$ and balance the convergence rate across different loss terms.

OceanPINN utilizes three loss terms: $\mathcal{L}_N$ ensures adherence to the governing equation, while $\mathcal{L}_M$ and $\mathcal{L}_B$ adjust the OceanPINN prediction at sampling points to match

ALGORITHM 1. Retain-Resample-Release (R3) sampling algorithm for OceanPINN.

1: Sample the initial population $\mathcal{P}_0$ of collocation points $\{x_n^i\}_{i=1}^{N_n}$ from a uniform distribution $U(\Omega)$
2: **for** $i = 0$ to max. iteration $- 1$ **do**
3:    Compute the real (R_r) and imaginary (R_i) PDE residuals of collocation points $x_n \in \mathcal{P}_i$
4:    Sort R_r and R_i
5:    Select populations $\mathcal{P}_{i,\text{real}}^r$ and $\mathcal{P}_{i,\text{imag}}^r$ such that satisfy top one-third R_r and R_i
6:    Merge two populations except overlapping $\mathcal{P}_i^r \leftarrow \mathcal{P}_{i,\text{real}}^r \cup \mathcal{P}_{i,\text{imag}}^r$
7:    Retain $\mathcal{P}_i^r$ and resample the population $\mathcal{P}_i^s$ from a uniform distribution $U(\Omega)$
8:    Merge the two population $\mathcal{P}_{i+1} \leftarrow \mathcal{P}_i^r \cup \mathcal{P}_i^s$
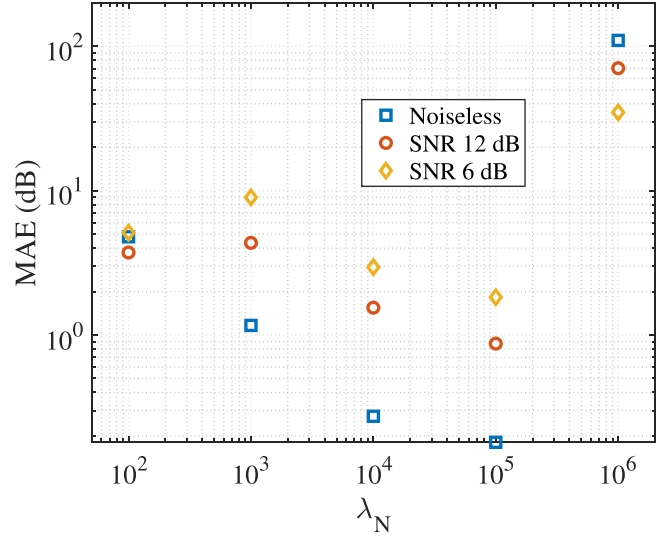9: **end for**

FIG. 10. (Color online) MAE (dB) of the OceanPINN predicted field's sound pressure level, trained with different λ_N and SWellEx-96 simulation data with different SNRs from Sec. IV A.

measured and surface pressures. The formulation of $\mathcal{L}_N$ deviates from the other two, potentially leading to discrepancies in gradient magnitudes. Considering these distinctions, we test various loss weight coefficients of $\lambda_N = \{10^2, 10^3, 10^4, 10^5, 10^6\}$, while setting $\lambda_M = \lambda_B = 1$. The best results are obtained from $\lambda_N = 10^5$ for every SWellEx-96 simulation in Sec. IV A, as shown in Fig. 10. $\lambda_N = 10^4$ also demonstrates predictions close to the true solution and $\lambda_N = 10^3$ yields favorable results in the noiseless scenario.

Figure 11 shows examples of predictive failure in the noiseless SWellEx-96 simulation scenario due to inappropriate λ_N values. As shown in Fig. 11(a), relatively low values of λ_N can lead OceanPINN to overfit at measured and surface points. In contrast, as depicted in Fig. 11(b), an overly high λ_N can lead OceanPINN to converge to trivial solutions, i.e., zero pressure field. This trivial solution satisfies the homogeneous Helmholtz equation, and can easily reduce $\mathcal{L}_N$, though not a meaningful solution. MAE in Fig. 10 is high for $\lambda_N = 10^6$ due to the pressure being close to zero.

At low SNR, the MAE increases with lower λ_N. This is attributed to a lower λ_N amplifying the impact of the reconstruction loss, which leads to overfitting to noisy measured data. However, a lower λ_N facilitates faster model
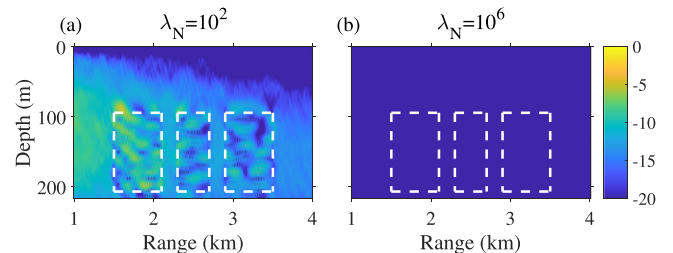

FIG. 11. (Color online) The normalized sound pressure level (dB) of OceanPINN predicted pressure field, which is trained with (a) $\lambda_N = 10^2$, (b) $\lambda_N = 10^6$.

convergence and improved stability. During the initial iterations, as predicted solutions significantly deviate from the true solution, the PDE loss becomes less effective. A lower λ_N enables the neural network to quickly align the values at measured and surface points. Future studies could investigate dynamic loss weight coefficients, starting with low λ_N that increases over iterations, to enhance convergence speed and performance. Further, adopting adaptive loss weight coefficients[60] could diminish the need to fine-tune these coefficients manually and enhance model performance.

[1]M. Raissi, P. Perdikaris, and G. E. Karniadakis, "Physics-informed neural networks: A deep learning framework for solving forward and inverse problems involving nonlinear partial differential equations," J. Comput. Phys. **378**, 686–707 (2019).

[2]A. B. Baggeroer, W. Kuperman, and H. Schmidt, "Matched field processing: Source localization in correlated noise as an optimum parameter estimation problem," J. Acoust. Soc. Am. **83**(2), 571–587 (1988).

[3]Z.-H. Michalopoulou and M. B. Porter, "Matched-field processing for broad-band source localization," IEEE J. Ocean. Eng. **21**(4), 384–392 (1996).

[4]G. Byun, F. Hunter Akins, K. L. Gemba, H. Song, and W. Kuperman, "Multiple constraint matched field processing tolerant to array tilt mismatch," J. Acoust. Soc. Am. **147**(2), 1231–1238 (2020).

[5]L. Sha and L. W. Nolte, "Bayesian sonar detection performance prediction with source position uncertainty using SWellEx-96 vertical array data," IEEE J. Ocean. Eng. **31**(2), 345–355 (2006).

[6]S. An, K. Lee, and W. Seong, "Optimal operating depth search for active towed array sonar using simulated annealing," Def. Sci. J. **69**(4), 415–419 (2019).

[7]C. M. Duarte, L. Chapuis, S. P. Collin, D. P. Costa, R. P. Devassy, V. M. Eguiluz, C. Erbe, T. A. Gordon, B. S. Halpern, H. R. Harding, Havlik, M. N., Meekan, M., Merchant, N. D., Miksis-Olds, J. L., Parsons, M., Predragovic, M., Radford, A. N., Radford, C. A., Simpson, S. D., Slabbekoorn, H., Staaterman, E., Van Opzeeland, I. C., Winderen, J., Zhang, X., and Juanes, F. "The soundscape of the anthropocene ocean," Science **371**(6529), eaba4658 (2021).

[8]C. Erbe, S. A. Marley, R. P. Schoeman, J. N. Smith, L. E. Trigg, and C. B. Embling, "The effects of ship noise on marine mammals–A review," Front. Mar. Sci. **6**, 606 (2019).

[9]H. Niu, E. Reeves, and P. Gerstoft, "Source localization in an ocean waveguide using supervised machine learning," J. Acoust. Soc. Am. **142**(3), 1176–1188 (2017).

[10]S. Yoon, H. Yang, and W. Seong, "Deep learning-based high-frequency source depth estimation using a single sensor," J. Acoust. Soc. Am. **149**(3), 1454–1465 (2021).

[11]H. Niu, Z. Gong, E. Ozanich, P. Gerstoft, H. Wang, and Z. Li, "Deep-learning source localization using multi-frequency magnitude-only data," J. Acoust. Soc. Am. **146**(1), 211–222 (2019).

[12]M. J. Bianco, P. Gerstoft, J. Traer, E. Ozanich, M. A. Roch, S. Gannot, and C.-A. Deledalle, "Machine learning in acoustics: Theory and applications," J. Acoust. Soc. Am. **146**(5), 3590–3628 (2019).

[13]Y. Choo, K. Lee, W. Hong, S.-H. Byun, and H. Yang, "Active underwater target detection using a shallow neural network with spectrogram-based temporal variation features," IEEE J. Ocean. Eng. **49**, 279–293 (2022).

[14]X. Xiao, W. Wang, Q. Ren, P. Gerstoft, and L. Ma, "Underwater acoustic target recognition using attention-based deep neural network," JASA Express Lett. **1**(10), 106001 (2021).

[15]Z.-H. Michalopoulou, P. Gerstoft, B. Kostek, and M. A. Roch, "Introduction to the special issue on machine learning in acoustics," J. Acoust. Soc. Am. **150**(4), 3204–3210 (2021).

[16]A. Varon, J. Mars, and J. Bonnel, "Approximation of modal wavenumbers and group speeds in an oceanic waveguide using a neural network," JASA Express Lett. **3**(6), 066003 (2023).

[17]J. Jin, P. Saha, N. Durofchalk, S. Mukhopadhyay, J. Romberg, and K. G. Sabra, "Machine learning approaches for ray-based ocean acoustic tomography," J. Acoust. Soc. Am. **152**(6), 3768–3788 (2022).

[18]C. D. Escobar-Amado, T. B. Neilsen, J. A. Castro-Correa, D. F. Van Komen, M. Badiey, D. P. Knobles, and W. S. Hodgkiss, "Seabed classification from merchant ship-radiated noise using a physics-based ensemble of deep learning algorithms," J. Acoust. Soc. Am. **150**(2), 1434–1447 (2021).

[19]R. A. McCarthy, S. T. Merrifield, J. Sarkar, and E. J. Terrill, "Reduced-order machine-learning model for transmission loss prediction in underwater acoustics," IEEE J. Ocean. Eng. **48**(4), 1149–1173 (2023).

[20]X. Li, P. Wang, W. Song, and W. Gao, "Modal wavenumber estimation by combining physical informed neural network," J. Acoust. Soc. Am. **153**(5), 2637–2648 (2023).

[21]K. Li and M. Chitre, "Data-aided underwater acoustic ray propagation modeling," IEEE J. Ocean. Eng. **48**, 1127–1148 (2023).

[22]K. Li and M. Chitre, "Physics-aided data-driven modal ocean acoustic propagation modeling," in *Proceedings of the International Congress on Acoustics*, Gyeongju, Korea (October 24–28, 2022) (International Commission for Acoustics, Madrid, Spain, 2022), pp. 1–9, available at https://www.icacommission.org/.

[23]L. Du, Z. Wang, Z. Lv, L. Wang, and D. Han, "Research on underwater acoustic field prediction method based on physics-informed neural network," Front. Mar. Sci. **10**, 1302077 (2023).

[24]S. Karimpouli and P. Tahmasebi, "Physics informed machine learning: Seismic wave equation," Geosci. Front. **11**(6), 1993–2001 (2020).

[25]M. Raissi, A. Yazdani, and G. E. Karniadakis, "Hidden fluid mechanics: Learning velocity and pressure fields from flow visualizations," Science **367**(6481), 1026–1030 (2020).

[26]G. Kissas, Y. Yang, E. Hwuang, W. R. Witschey, J. A. Detre, and P. Perdikaris, "Machine learning in cardiovascular flows modeling: Predicting arterial blood pressure from non-invasive 4D flow MRI data using physics-informed neural networks," Comput. Methods Appl. Mech. Eng. **358**, 112623 (2020).

[27]C. Song, T. Alkhalifah, and U. B. Waheed, "A versatile framework to solve the Helmholtz equation using physics-informed neural networks," Geophys. J. Int. **228**(3), 1750–1762 (2022).

[28]X. Huang and T. Alkhalifah, "PINNup: Robust neural network wavefield solutions using frequency upscaling and neuron splitting," J. Geophys. Res. Solid Earth **127**(6), e2021JB023703, https://doi.org/10.1029/2021JB023703 (2022).

[29]U. B. Waheed, "Kronecker neural networks overcome spectral bias for PINN-based wavefield computation," IEEE Geosci. Remote Sens. Lett. **19**, 8029805(2022).

[30]M. Rasht-Behesht, C. Huber, K. Shukla, and G. E. Karniadakis, "Physics-informed neural networks (PINNs) for wave propagation and full waveform inversions," J. Geophys. Res. Solid Earth **127**(5), e2021JB023120, https://doi.org/10.1029/2021JB023120 (2022).

[31]N. Borrel-Jensen, A. P. Engsig-Karup, and C.-H. Jeong, "Physics-informed neural networks for one-dimensional sound field predictions with parameterized sources and impedance boundaries," JASA Express Lett. **1**(12), 122402 (2021).

[32]S. Wang, X. Yu, and P. Perdikaris, "When and why PINNs fail to train: A neural tangent kernel perspective," J. Comput. Phys. **449**, 110768 (2022).

[33]A. Krishnapriyan, A. Gholami, S. Zhe, R. Kirby, and M. W. Mahoney, "Characterizing possible failure modes in physics-informed neural networks," Adv. Neural Inf. Process. Syst. **34**, 26548–26560 (2021).

[34]N. Rahaman, A. Baratin, D. Arpit, F. Draxler, M. Lin, F. Hamprecht, Y. Bengio, and A. Courville, "On the spectral bias of neural networks," in *International Conference on Machine Learning* (PMLR, 2019), pp. 5301–5310, available at https://proceedings.mlr.press/.

[35]A. Jacot, F. Gabriel, and C. Hongler, "Neural tangent kernel: Convergence and generalization in neural networks," Adv. Neural Inf. Process. Syst. **31**, 1–10 (2018).

[36]S. Wang, H. Wang, and P. Perdikaris, "On the eigenvector bias of Fourier feature networks: From regression to solving multi-scale PDEs with physics-informed neural networks," Comput. Methods Appl. Mech. Eng. **384**, 113938 (2021).

[37]F. B. Jensen, W. A. Kuperman, M. B. Porter, H. Schmidt, and A. Tolstoy, *Computational Ocean Acoustics* (Springer, New York, 2011), Vol. 2011.

[38]P. Gerstoft, "Inversion of seismoacoustic data using genetic algorithms and *a posteriori* probability distributions," J. Acoust. Soc. Am. **95**(2), 770–782 (1994).

[39]D. F. Gingras and P. Gerstoft, "Inversion for geometric and geoacoustic parameters in shallow water: Experimental results," J. Acoust. Soc. Am. **97**(6), 3589–3598 (1995).

[40]D. J. Battle, P. Gerstoft, W. A. Kuperman, W. S. Hodgkiss, and M. Siderius, "Geoacoustic inversion of tow-ship noise via near-field-matched-field processing," IEEE J. Ocean. Eng. **28**(3), 454–467 (2003).

[41]N. R. Chapman and E. C. Shang, "Review of geoacoustic inversion in underwater acoustics," J. Theor. Comput. Acoust. **29**(03), 2130004 (2021).

[42]J. Bonnel, S. P. Pecknold, P. C. Hines, and N. R. Chapman, "An experimental benchmark for geoacoustic inversion methods," IEEE J. Ocean. Eng. **46**(1), 261–282 (2021).

[43]T. C. Yang, "Source depth estimation based on synthetic aperture beamfoming for a moving source," J. Acoust. Soc. Am. **138**(3), 1678–1686 (2015).

[44]S. Walker, P. Roux, and W. A. Kuperman, "Modal Doppler theory of an arbitrarily accelerating continuous-wave source applied to mode extraction in the oceanic waveguide," J. Acoust. Soc. Am. **122**(3), 1426–1439 (2007).

[45]N. O. Booth, P. A. Baxley, J. Rice, P. Schey, W. Hodgkiss, G. D'Spain, and J. Murray, "Source localization with broad-band matched-field processing in shallow water," IEEE J. Ocean. Eng. **21**(4), 402–412 (1996).

[46]G. D'spain, J. Murray, W. Hodgkiss, N. Booth, and P. Schey, "Mirages in shallow water matched field processing," J. Acoust. Soc. Am. **105**(6), 3245–3265 (1999).

[47]M. B. Porter, "The KRAKEN normal mode program," Naval Res. Lab, Washington, DC, 1992.

[48]K. Hornik, M. Stinchcombe, and H. White, "Multilayer feedforward networks are universal approximators," Neural Netw. **2**(5), 359–366 (1989).

[49]A. G. Baydin, B. A. Pearlmutter, A. A. Radul, and J. M. Siskind, "Automatic differentiation in machine learning: A survey," J. Mach. Learn. Res. **18**, 1–43 (2018).

[50]V. Sitzmann, J. Martel, A. Bergman, D. Lindell, and G. Wetzstein, "Implicit neural representations with periodic activation functions," Adv. Neural Inf. Process. Syst. **33**, 7462–7473 (2020).

[51]A. Daw, J. Bu, S. Wang, P. Perdikaris, and A. Karpatne, "Mitigating propagation failures in physics-informed neural networks using retain-resample-release (R3) sampling," in *Proceedings of the 40th International Conference on Machine Learning* Honolulu, HI (PMLR, 2023), Vol. 202, pp. 7264–7302, available at https://icml.cc/Conferences/2023.

[52]Y. Park, P. Gerstoft, and W. Seong, "Grid-free compressive mode extraction," J. Acoust. Soc. Am. **145**(3), 1427–1442 (2019).

[53]J. Kim, K. Lee, D. Lee, S. Y. Jhin, and N. Park, "DPM: A novel training method for physics-informed neural networks in extrapolation," Proc. AAAI Conf. Artif. Intell. **35**, 8146–8154 (2021).

[54]Y. Park, F. Meyer, and P. Gerstoft, "Graph-based sequential beamforming," J. Acoust. Soc. Am. **153**(1), 723–737 (2023).

[55]F. Hunter Akins and W. Kuperman, "Experimental demonstration of low signal-to-noise ratio matched field processing with a geoacoustic model extracted from noise," J. Acoust. Soc. Am. **153**(5), 2818–2825 (2023).

[56]Y. Park, F. Meyer, and P. Gerstoft, "Sequential sparse Bayesian learning for time-varying direction of arrival," J. Acoust. Soc. Am. **149**(3), 2089–2099 (2021).

[57]F. Meyer and K. L. Gemba, "Probabilistic focalization for shallow water localization," J. Acoust. Soc. Am. **150**(2), 1057–1066 (2021).

[58]K. L. Gemba, S. Nannuru, P. Gerstoft, and W. S. Hodgkiss, "Multi-frequency sparse Bayesian learning for robust matched field processing," J. Acoust. Soc. Am. **141**(5), 3411–3420 (2017).

[59]P. A. Baxley, N. O. Booth, and W. S. Hodgkiss, "Matched-field replica model optimization and bottom property inversion in shallow water," J. Acoust. Soc. Am. **107**(3), 1301–1323 (2000).

[60]S. Wang, Y. Teng, and P. Perdikaris, "Understanding and mitigating gradient flow pathologies in physics-informed neural networks," SIAM J. Sci. Comput. **43**(5), A3055–A3081 (2021).